HAL
open science

X-ray absorption spectroscopy and Eu3+-emission characteristics in GaAs/SnO2 heterostructure

Cristina Bueno, Aline Y. Ramos, Aude Bailly, Eric Mossang, Luis Scalvi

To cite this version:

Cristina Bueno, Aline Y. Ramos, Aude Bailly, Eric Mossang, Luis Scalvi. X-ray absorption spectroscopy and Eu3+-emission characteristics in GaAs/SnO2 heterostructure. SN Applied Sciences, 2020, 2 (9), pp.1579. 10.1007/s42452-020-03344-3 . hal-02936162

HAL Id: hal-02936162

https://hal.science/hal-02936162v1

Submitted on 9 Oct 2020

HAL is a multi-disciplinary open access archive for the deposit and dissemination of scientific research documents, whether they are published or not. The documents may come from teaching and research institutions in France or abroad, or from public or private research centers.

L'archive ouverte pluridisciplinaire **HAL**, est destinée au dépôt et à la diffusion de documents scientifiques de niveau recherche, publiés ou non, émanant des établissements d'enseignement et de recherche français ou étrangers, des laboratoires publics ou privés.

Manuscript

Click here to view linked References

Click here to access/download;Manuscript;paper Bueno et al SN Appl. Sci V3.docx

X-ray absorption spectroscopy and Eu^{3+}-emission characteristics in GaAs/SnO_2 heterostructure

Cristina F. Bueno[1], Aline Y. Ramos[2], Aude Bailly[2], Eric Mossang[2], Luis V. A. Scalvi[1*]

[1] *UNESP – São Paulo State University, Physics Dept.– FC and POSMAT – Post-Graduate Program in Materials Science and Technology, Bauru – SP, Brazil*

[2]*Institut Néel, Université Grenoble Alpes, CNRS, Grenoble 38042, France*

(*) Corresponding author: luis.scalvi@unesp.br

Abstract

X-ray absorption near edge structure (XANES) and extended X-ray absorption fine structure (EXAFS) data are used for investigating heterostructure samples of GaAs/SnO_2. XANES data are used for analyzing the local organization around Eu in the heterostructure formed by GaAs and Eu-doped SnO_2. The differences between the XANES data for these samples and data obtained for Eu-doped SnO_2 thin films, deposited on glass substrate, is assumed as responsible for the differences in the photoluminescence (PL) spectra concerning the Eu^{3+} emission, since films deposited on glass substrate does not present Eu^{3+} PL transitions until the annealing temperature is rather high. Eu^{3+} emission is explored using two different excitation sources: 350 nm from a Kr^+ laser (above SnO_2 energy bandgap) and 488 nm from an Ar^+ laser (below SnO_2 bandgap energy). The existence of more organized regions around the Eu^{3+} site, observed for the heterostructure surface may be associated with the Eu^{3+} luminescent emission. The main and secondary features in the XANES show that there are differences in the average local Eu environment for the SnO_2:Eu isolated thin films and heterostructures, being more organized in the latter. Electrical characterization evidences that the portion of the resistivity reduction that corresponds to photo-ionized intrabandgap states is responsible for the persistent photoconductivity phenomenon in the heterostructures.

1. Introduction

There is currently great interest in semiconductor oxides and their heterostructures due to their potential applications in spintronic devices [1], photocatalysis [2], light emitting diodes, lasers [3] and solar cells [4]. Tin dioxide (SnO_2) is one of the most used semiconductor oxides, related to outstanding properties such as high transparency in the visible range, high reflectivity in the infrared [5] and high n-type free carrier concentration [6], even in the undoped form, which may lead to a high conductivity when electron scattering phenomena are prevented. Doped SnO_2 thin films are used as transparent electrodes in several systems: perovskite solar cells [7], lithium-ion batteries [8] and organic photovoltaic cells [9]. The interest in doping semiconductor oxides with rare-earth (RE) ions has increased considerably, due to its radiative emissions over a large wavelength range, which allows several types of applications such as LEDs, displays, telecommunications, analytical sensors, biomedical images [10]. Its properties depend on the location of the rare-earth ion incorporation within the crystalline lattice of the matrix [11].

X-ray Absorption Near Edge Structure (XANES) are the features up to 50 eV after the absorption edge, being strongly sensitive to oxidation state and coordination chemistry of the absorber atom [12]. Amidani and coworkers [13] employed X-ray Absorption Spectroscopy (XAS) to understand the degradation process at atomic level in Eu^{2+} doped $BaMgAl_{10}O_{17}$. Data of HERFD (High Energy Resolution Fluorescence Detected)-XANES yielded stable structural properties of the host lattice upon irradiation, and rapid oxidation of Eu^{2+} to Eu^{3+}. Analysis of OH^--free Eu-doped aluminosilicate compounds, concerning the surrounding of Eu crystal field, leads to the conclusion that the oxidation states influence the luminescent properties [14]. XANES showed a hybrid structure (Eu^{2+} and Eu^{3+} oxidation states): the higher the silica concentration, the more efficient the conversion Eu^{2+}/Eu^{3+}, which was associated with non-bridging oxygen amount and matrix optical basicity changes. Grzeta and coworkers [15] have determined the oxidation state of Eu doping and the coordination within the $BaAl_2O_4$ host structure. XANES of Eu-doped $BaAl_2O_4$ confirmed the 3+ oxidation state for europium, while EXAFS studies provided evidence that the structure of this

sort of sample is quite similar to undoped $BaAl_2O_4$, where Eu^{3+} substitutes Ba^{2+}, besides confirming the presence of interstitial oxygen. The coexistence of europium doping (divalent and trivalent ions) in Ga_2O_3 nanocrystals was demonstrated by Layek and coworkers [16]. Eu^{3+}, partly located in the nanocrystal surface region, reduced to Eu^{2+}, is internally stabilized when samples were exposed to X-ray radiation, being an alternative approach for oxidation state manipulation and a potential application of Ga_2O_3 as an X-ray storage phosphor. Europium oxidation state was investigated by XANES concerning the dependency on external and chemical pressure in $Ca_{1-x}Eu_xCo_2As_2$ [17]. The Eu valence increases with pressure and Ca concentration, agreeing with *f-d* hybridization in determination of the electronic structure; besides it changes almost linearly with applied pressure. The chemical pressure exerts a very weak influence on the Eu valence (compared with the external pressure), what leads to $EuCo_2As_2$ crystal lattice softness.

Rare-earth doping presents high quantum efficiency on the photoluminescence (PL) when incorporated into wide bandgap semiconductors [18]. However, they affect significantly the electrical transport in oxide semiconductor due to the acceptor-like behavior. Considering that SnO_2 is a naturally n-type semiconductor, the doping with Eu^{3+} ions leads to high charge compensation since the Eu^{3+} acceptors-like impurities trap the lattice frees electrons, which decreases the film conductivity. The Eu^{3+} incorporated in SnO_2 has its PL structure highly dependent on the ion location: when the ions are mostly located at substitutional Sn sites the Eu^{3+} transition $^5D_0 \rightarrow {}^7F_1$ occurs preferentially, while the $^5D_0 \rightarrow {}^7F_2$ transition is dominant when the ions are located at asymmetric sites, specifically grain boundary layers [19].

The Eu^{3+} emission can be significantly facilitated in the heterostructure $GaAs/SnO_2$ [20], assembly that may also provide electrical properties advances [21-24]. Then, in order to understand the rule for PL emission on these heterostructure samples, PL is carried out with above SnO_2 bandgap light (energy transfer from the matrix) as well as below bandgap energy, by direct Eu^{3+} excitation. Besides, XAFS measurements are carried out and the interpretation reveals the local Eu^{3+} neighborhood, which may be responsible for the emission even for lower annealing temperatures, and is more organized in the case of heterostructure $GaAs/SnO_2$. It leads to regions

where the Eu^{3+} emission is more easily accomplished. Moreover, photo-induced current decay data for different temperatures, excited with below and above SnO_2 bandgap light energies, reveals the possible confinement of electrons at the heterostructure interface region and that the persistent photoconductivity (PPC) phenomenon comes from intrabandgap states in the SnO_2 top layer [25,26], which presents typically local lattice relaxation.

Moreover, in SnO_2, several sorts of PL emission may be present related to the matrix itself. PL spectra of SnO_2:Sb films showed peculiar PL structure in the range 390 nm to 520 nm [27]. In this PL emission range, a UV-violet peak about 390 nm can be associated to the electron transition between vacancy donor levels and acceptor levels formed by Sb ions [27]. It is interesting to note that in the case of the material investigated in the present paper the acceptor level would be formed by Eu ions, which in the trivalent oxidation state (Eu^{3+}) is much more suitable to form acceptor-like defects than Sb, which presents contributions of Sb^{3+} and Sb^{5+} oxidation states [28]. As can be seen the broader band is clearly present in our data and is highly dependent on the thermal annealing temperature. The origin of this band has been the issue of another publication [20] and it will not be treated here.

The aim here is to provide knowledge on structural properties that may be related to the Eu^{3+} emission on this sort of heterostructure in the form of thin films, along with photo-induced transport properties, in order to gain expertise in this sort of film assembly, very desirable for optoelectronic applications.

2. Experimental details

2.1 Thin film deposition

Thin films of gallium arsenide were resistively evaporated using an Edwards AUTO 500 evaporator system. The technique consists on placing small pieces of the material GaAs inside a metallic boat (tungsten), and the evaporation takes place through the passage of high electric current

in the boat, which heats up by the Joule effect in a low-pressure chamber (~ 10^{-5} mbar). After the deposition the films were treated at 150°C by 30 min in air atmosphere in an EDGCON 3P oven.

The deposition of Eu^{3+}-doped SnO_2 thin film layer has been detailed previously [19]. The film growth is done at room temperature and air atmospheric conditions. The samples are dried in air by 20 min and thermally treated at 200°C by 10 min after each layer. This procedure is repeated 10 times for the formation of a 10 layers deposited sample. The final annealing was at 200°C by 1 hour (samples with 0.05, 0.1 and 2at%Eu) or 400°C by 20 min (2at%Eu). SnO_2:Eu thin film was deposited directly on soda-lime glass or quartz substrate, and the final annealing was 500°C (0.05, 0.1 and 2at%Eu) and 1000°C by 1 hour, respectively. Another sample is also done with the remaining powder of SnO_2:2at%Eu, resulting from the evaporation of solvent from the precursor solution. This powder was pressed down with 5000 kgf/cm^2 by 3 min to form a pellet, and treated at 1000°C by 20 min.

2.2 X-ray absorption spectroscopy (XAS)

High energy resolution fluorescence detected - X-ray absorption spectroscopy (HERFD-XAS) data have been collected at the Eu L_3-edge (6977 eV) at the BM16 beamline of European Synchrotron Radiation Facility (ESRF – Grenoble, France) [29]. The XANES (X-ray absorption near edge structure) spectra were collected in grazing incident geometry (10-15 deg), in fluorescence mode, using a crystal analyzer spectrometer with bent Ge 111 crystals and single-element silicon drift diode detector. The GaAs/SnO_2:Eu heterostructure samples and Eu-doped SnO_2 thin films were cut into pieces with a length of about 2.0 cm and a width of 1.0 cm. Then, they were cleaned with ethyl alcohol to remove any impurity from the surface. Thus, the samples were attached to the equipment to perform the measurement. Absorption spectra were also measured using the XAFS2 beamline of the Brazilian Synchrotron Light Laboratory (LNLS – Campinas, Brazil) [30], and the XANES spectra were collected in fluorescence mode, using a Canberra Ge-15 solid state detector. For XAS analysis, the XANES spectra have been normalized

by eliminating the signal of residual absorption (μ_0), due to all elements located in the beam path in the sample. Thus, the pre-edge region was removed from the spectrum, eliminating the curve formed in the spectrum by the linear extrapolation in that region. Then, the atomic absorption (μ_1) of the studied atom was extracted by simulating in the post-edge region by a degree 4 or 5 polynomial, this polynomial being intermediate to the EXAFS oscillations. Normalized XANES spectra were analyzed comparing with Eu_2O_3 reference to determine the Eu oxidation in the Eu-doped SnO_2 thin films. Data analysis was done through data processing in Demeter [31] system, using the Athena (XANES analysis) and Artemis (EXAFS analysis) softwares.

2.3 Photoluminescence

Photoluminescence (PL) measurements were carried out with the excitation of a modulated Kripton (Kr^+) laser (350 nm line) and the detection of signal was done by a R955 PMT from Hamamatsu. A SR530 Lock-in Amplifier from Stanford Research System was also used and a single configuration monochromator was used for PL spectra scanning. The 488 nm excited PL experiments were done with an Argon (Ar^+) laser, and were carried out in the backscattering geometry and all spectra were corrected by the diffraction grating and CCD detector optical responses.

The Raman measurements were obtained from a commercial setup (Renishaw RM2000) by exciting the samples with 632.8 nm laser radiation, with no preferential polarization. In all cases, the measurements were performed at room-temperature and great care was taken to avoid sample heating.

2.4 Scanning electron microscopy (SEM) measurements

Morphological characterization was carried out with a field emission scanning electron microscopy (FESEM) Zeiss Ultra Plus, using secondary electron detector, at Institut Néel, Grenoble-France, and SEM Carl Zeiss model LS15, at UNESP, Bauru-Brazil.

2.5 X-ray Diffraction

X-ray diffraction patterns were measured in a Rigaku diffractometer, model D/MAX 2100PC operated with a Cu K_α radiation source (1.5405 Å) and a Ni filter for reducing the K_β radiation. Data were collected with 0.02° of step and scanning rate of 1°/min in the 2theta mode for films (fixed incident angle of 1.5°) in the angular region of $20° \leq 2\theta \leq 90°$.

2.6 Electrical characterization

Electrical contacts were deposited to the GaAs/SnO_2:2%Eu heterostructure surface, and were accomplished by deposition of metallic indium also by resistive evaporation. The sample with electrical contacts was submitted to annealing at 150°C by 30 min. Current-voltage in the dark was carried out using an electrometer from Keithley model 6517. The system used for GaAs/SnO_2:2%Eu sample measurements was a Janis He-closed cycle cryostat with a compressor CTI-Cryogenics, coupled to a temperature controller from Lake-Shore. The heterostructure was irradiated with He-Cd laser (325 nm, 3.82 eV) and InGaN LED (450 nm, 2.76 eV) with the temperature controlled at 50 or 200 K, until current saturation. Then the light is shut off and the optically generated current decay as function of time is recorded, keeping the applied voltage as 5 V, as published previously [25]. The current-voltage after this decay is recorded again and reported here.

3. Results and Discussion

3.1 Structural characterization

Scanning electron microscopy (SEM) surface images of GaAs/SnO_2:2at%Eu heterostructure has revealed the possibility of Eu agglomerates on the surface of this sample [20]. SEM images specific of the samples used in this work are shown in Figure 1: GaAs bottom layer, Eu-doped SnO_2 film, grown on soda-lime glass substrate and heterostructures surfaces. Fig. 1(a) shows the GaAs

surface, where it is possible to observe that it is homogeneous, but with the existence of particles (agglomerates), resembling nanosized balls (about 300 nm). The image for SnO_2:2at%Eu film surface is presented in Fig. 1(b), and shows a more uniform surface when compared to the GaAs film (Fig. 1(a)). The surface micrographs of the samples of the heterostructure GaAs/SnO_2:2%Eu with thermal annealing of 200°C/1 hour (Fig. 1(c) and (d)), show the presence of particles (agglomerates) on the surface of these films, similar to the thin film of GaAs deposited directly on the glass substrate, and similar to the heterostucture SEM images reported previously [20,23]. However, these heterostructures also present regions similar to the SnO_2 film, as if the SnO_2 deposition better covered the bottom layer (GaAs), whereas for the regions showing the particles (nanosized agglomerates) on the film surface, the deposition of the top layer (SnO_2) probably did not cover completely the bottom layer. Fig. 1(f) is a (field emission) FESEM image of GaAs/SnO_2:2%Eu heterostructure annealed at 400°C/20 min, and reveals some of these peculiarities (regions not completely covered by SnO_2). Although the isolated film surface is apparently more homogeneous, the existence of sites with differences in the Eu neighborhood configuration as well as in the secondary structures may justify the PL emission more likely in the tiny balls present in the GaAs/SnO_2:Eu heterostructure surface. It may also change the vicinity configuration and structural arrangement, which in turn favors the characteristic emission peaks of Eu. Then, the presence of GaAs as bottom layer also provides a more suitable arrangement for luminescence.

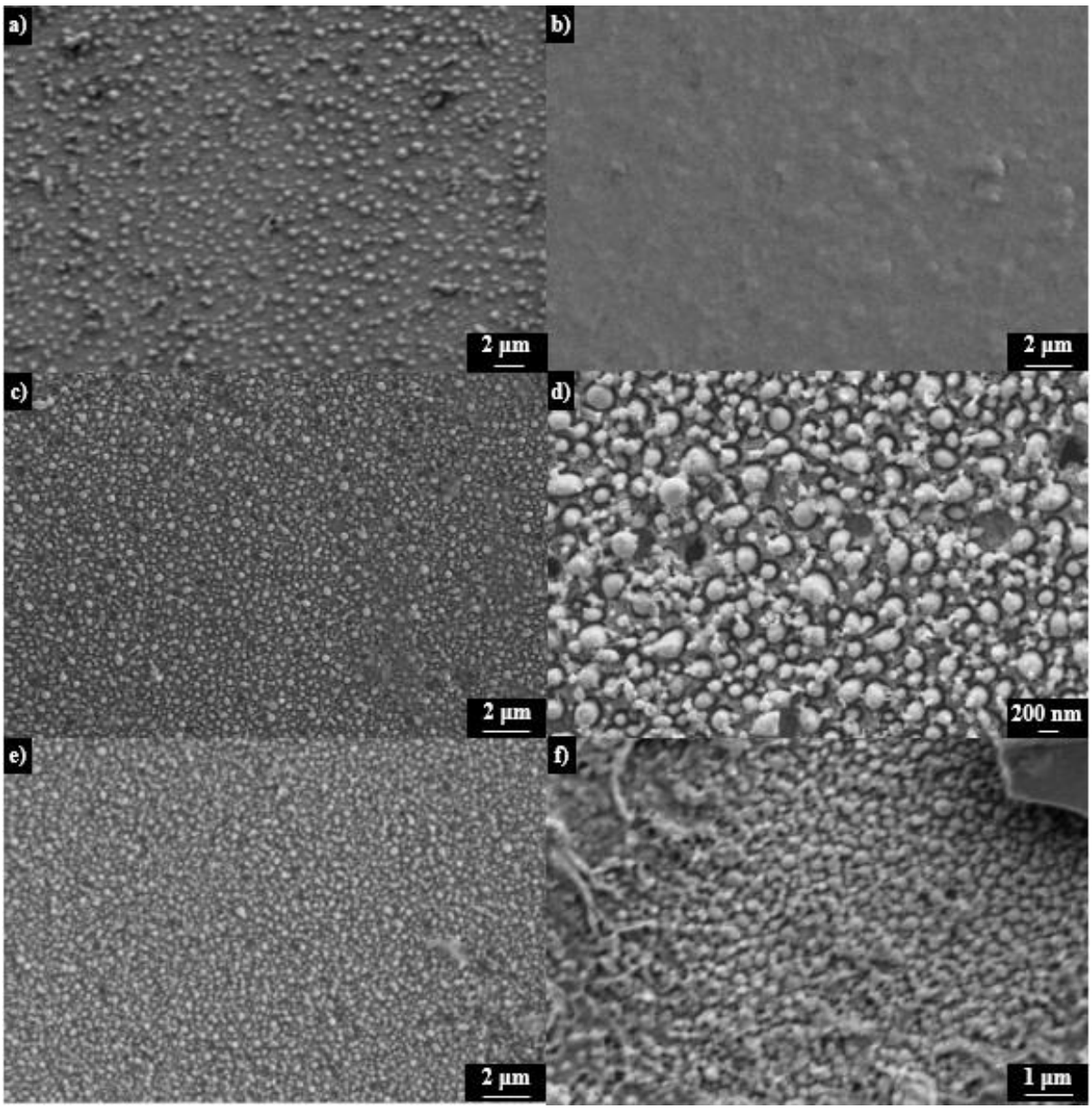

Fig 1. Surface images for: **(a)** GaAs thin film (FESEM- scale bar: 2 µm), **(b)** SnO_2:2%Eu thin film (SEM- scale bar: 2 µm); **(c)** heterostructure GaAs/SnO_2:2%Eu annealed at 200°C/1 hour (SEM- scale bar : 2 µm) **(d)** GaAs/SnO_2:2%Eu annealed at 200°C/1 hour (FESEM- scale bar: 200 nm) **(e)** GaAs/SnO_2:2%Eu annealed at 400°C/20 min (SEM- scale bar: 2 µm). **(f)** GaAs/SnO_2:2%Eu annealed at 400°C/20 min (FESEM- scale bar: 1 µm).

Fig.2 shows XANES spectra for the heterostructure for the sample series of GaAs/SnO_2:Eu heterostructures measured at BM16 beam line of European Synchrotron Radiation Facility (ESRF – Grenoble, France), as well as SnO_2:Eu thin films with three different doping concentration (0.05, 0.1 e 2at%). In GaAs/SnO_2:Eu the top layer is treated at 200°C/1 h and for the SnO_2:Eu thin film treated at 500°C/1 h. There is practically no difference within a series, however it is clearly

observed differences between the series of heterostructures and SnO_2 thin films. The peak at 6982.8 eV ("white line") is associated to electronic transition $2p_{3/2}$-5d [32,33]. The energy position of this line confirms that the Eu atom remains in the trivalent oxidation state after solution synthesis and film deposition, independently of the bottom layer (glass or GaAs). The total area under this white line, related to the number of empty 5d states, is the same for all samples. However, this line is higher and thinner for the heterostructure that for the SnO_2 doped film, indicating more localized levels. The same area suggests that the electronic configuration of Eu atoms is similar in films and heterostructures, while thinner and higher lines indicate that the average site of the Eu are more symmetric in the heterostructures. The area evaluation was done through a numerical integration procedure, where a pair of adjacent values is used to form a trapezoid for approximating the area beneath the segment of the curve defined by two points. The calculated area was restricted only to the absorption band and delimited by a horizontal baseline $[f(x_0)]$ chosen from a practically constant value of energy, just after this band. Then, the area was calculated through the equation:

$$\int_{x_1}^{x_n}[f(x)-f(x_0)]dx \approx \sum_{i=1}^{n-1}(x_{i+1}-x_i)\frac{1}{2}\{[f(x_{i+1})-f(x_0)]+[f(x_i)-f(x_0)]\}. \qquad (1)$$

The inset in Fig. 2 shows that some differences are also observed in the smooth features above the absorption edge that are related to the neighborhood of the Eu sites. *Ab-initio* simulations have shown that the radial distance Eu-O for heterostructure is higher than in the SnO_2 film, besides there are differences in second neighbors in each structure.

Fig. 2 allows concluding that the main and secondary features in the XANES show that there are differences in the Eu site configuration (or in the average local Eu environment) for the SnO_2:Eu thin films and heterostructures.

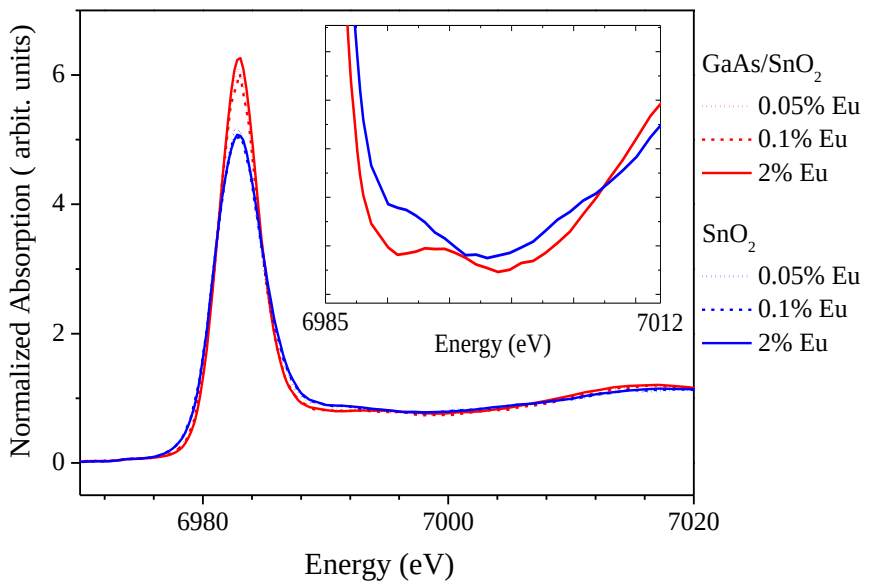

Fig. 2. XANES comparison between GaAs/SnO_2:Eu heterostructures and SnO_2:Eu films. The white line is found at the same value (6982.8 eV). **Inset**: Differences are very clear in the secondary's structures just above the absorption edge energy.

Simulations were done for the Eu1 neighbors' location in the Eu_2O_3 structure for data obtained at the LNLS (Brazilian Synchrotron Light Laboratory – Campinas, Brazil). The europium atom chosen as the origin in the simulation, designated as Eu1, has the position $\left(\frac{1}{2},\frac{1}{2},\frac{1}{2}\right)$ of the space group Ia-3 of Eu_2O_3 cubic crystalline system. All the parameters used to fit the first coordination shell for the GaAs/SnO_2:2%Eu heterostructure treated at 200°C, powder and film of SnO_2:2%Eu and Eu_2O_3 are summarized in Table 1. Two peaks are present in the simulation: the 6-oxygen coordination shell, distances between 2.20 to 2.40 Å (in our simulation, it results a peak about 1.9 Å) and a second shell of 12 europium neighbors, distances between 3.60 to 4.10 Å (in our simulation, peak about 3.8 Å). The analysis from the simulation may be extended to the isolated SnO_2 film samples and heterostructures. It leads to the observation that in the SnO_2:2%Eu film and powder the peak presence at about 3.8 Å position (Figure 3) suggests a few second Eu neighbors in the structure of each sample, even though this contribution is very low. However, this peak does not exist in the GaAs/SnO_2:2%Eu heterostructure, thus suggesting different second neighbors for SnO_2:2%Eu deposited on GaAs and for SnO_2:2%Eu isolated films and powders. However, the

identification of the heterostructure second neighbor is not possible because of the XAFS data (due to the difficulty of measuring a component samples were it has diluted concentration, in the form of films, thus presenting a noisy signal), and therefore the subsequent extraction of EXAFS did not result in data extending over an energy wide range after the absorption edge, that would allow second neighbor analysis. Then, at this point it is not possible to propose models for each site, even though in a previous paper [20], we have associated it with concentrated Eu regions.

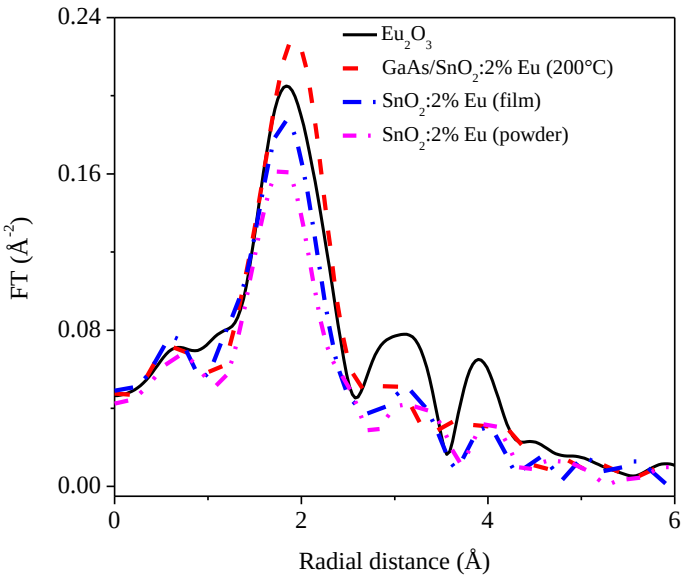

Fig. 3. Simulated Fourier transform for Eu_2O_3 reference, heterostructure, 2%Eu-doped film and powder.

Table 1 –Simulated parameters of Fourier transform used for Eu_2O_3 reference, heterostructure, 2%Eu-doped film and powder.

Coordination number (*N*)	**Debye-Waller factor (σ^2) (Å^2)**	**EXAFS $\chi(k)$ data range (Δk) (Å^{-1})**	**Fourier transform range (ΔR) (Å)**	**Eu-O interatomic distance (*R*) (Å)**
6	0.006-0.016	2.655-10.000	1.15-2.60	2.35-2.42

Figure 4 shows X-ray diffractograms for GaAs/SnO_2:Eu heterostructures, along with the identification of crystallographic planes. Figures 4(a) and (d) (SnO_2 top layer doped with 0.05%Eu (treated at 200°C) and 2%Eu (400°C), respectively), allow identification of three peaks characteristic of GaAs planes, and, two SnO_2 peaks. In Fig. 4(b) and (c) (heterostructures where the

SnO_2 layer is doped with 0.1 e 2%Eu, respectively, both treated at 200°C), it is possible to find three peaks characteristic of GaAs planes, besides the three peaks related to SnO_2. It is interesting to notice that in all the figures, the GaAs peaks are more intense than the SnO_2 peaks, and the peak located at 27.25° is the most intense for all the heterostructures. This peak is located very close to characteristic peaks of GaAs and SnO_2: (111) at 27.31° and (110) at 26.61°, respectively. The peak related to planes (110) of SnO_2 although it is reported as the most intense [34], for films deposited directly on glass the plane (101) is the most intense peak [20]. So, the experimental peak at 27.25° in Fig. 4 tends to belong to GaAs, because it is the most intense when GaAs films are deposited directly on glass substrate.

Concerning the SnO_2 peaks (Fig. 4(c) and (d)) the band width at half maximum decreases with temperature rise, leading to increase in the crystallite size. On the other hand, for GaAs, this parameter remains practically the same. It suggests that the thermal annealing may influence the most external layer (SnO_2), leaving the GaAs bottom layer practically unchanged.

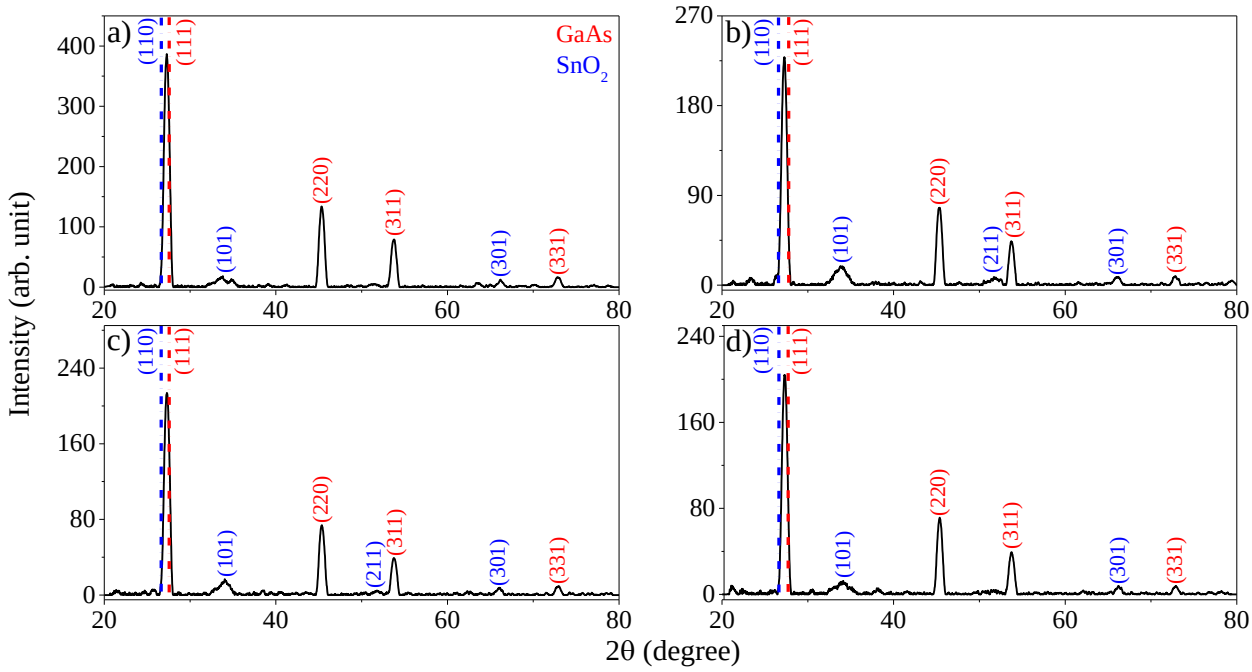

Fig. 4. X-ray diffractograms for heterostructures with thermal annealing at 200°C/1 h: **(a)** GaAs/SnO_2:0.05%Eu, **(b)** GaAs/SnO_2:0.1%Eu and **(c)** GaAs/SnO_2:2%Eu. **(d)** GaAs/SnO_2:2%Eu with thermal annealing at 400°C/20 min. Labeled crystalline planes refer to files JCPDS 32-0389 (GaAs, cubic) [35] and JCPDS 41-1445 (SnO_2, tetragonal, rutile) [35].

3.2 Photoluminescence data

Fig. 5(a) is the PL data in the energy range 1.9 to 2.2 eV, for excitation with a Kr^+ laser (350 nm, 3.53 eV) which is above the SnO_2 bandgap. The energy range in the figure is where the most relevant transitions of Eu^{3+} ion are located. In this figure, PL for the heterostructure GaAs/SnO_2:2at%Eu with distinct thermal annealing of the top SnO_2 film, as described in the experimental section, is presented, along with PL for SnO_2:2%Eu film with thermal annealing at 1000°C (quartz substrate). It is important to mention that isolated SnO_2 films deposited on glass substrate, and annealed at 500ºC does not show Eu^{3+} emission lines [20]. All of these spectra are normalized by the maximum intensity in order to demonstrate the relative position of the observed bands, and not to compare their intensities. PL for a powder sample of SnO_2, treated at 1000ºC is also shown.

Fig. 5(b) represents PL data for heterostructure GaAs/SnO_2:2at%Eu, for excitation with Kr^+ laser, where the top layer is treated for 1 h at distinct temperatures, in the range 200-500ºC. In this figure, a broad band and well-defined Eu^{3+} peaks are seen. This broad band has already been discussed in a previous publication and may be associated with electron transition between the vacancy donor level and the acceptor level formed by Eu^{3+} ions [20]. The blue shift observed previously in this broad band with annealing temperature [20] is also confirmed in Fig. 5(b), and can be also related to the crystallite size. As the crystallite decreases, the energy of the band gap becomes larger [36], thus the increasing disorder in the vicinity of defects creates a larger distribution in the levels of intrabandgap defects. Therefore, the broader distribution of levels caused by the more disordered neighborhood around both types of defects (the band is caused by electronic transfer between oxygen vacancies and Eu^{3+} levels), leads to a lower average transition energy for smaller crystallites [20], even for larger bandgap.

Concerning the Eu^{3+} transitions, the most relevant are: $^5D_0 \rightarrow {}^7F_1$ (about 2.1 eV) and $^5D_0 \rightarrow {}^7F_2$ (about 2.0 eV), which are clearly shown in Fig. 5(a), and are obtained by energy transfer from the SnO_2 matrix [19], considering the above band gap energy of the Kr^+ laser. The relative intensity of the transitions $^5D_0 \rightarrow {}^7F_1$ and $^5D_0 \rightarrow {}^7F_2$ seems to be changed as the temperature increases.

For the heterostructure samples where the SnO_2 layer is treated at 200ºC and 400ºC, the transition $^5D_0 \rightarrow {}^7F_2$ is the most intense, whereas for the samples treated at 1000ºC the $^5D_0 \rightarrow {}^7F_1$ is clearly the most intense. Even comparing the heterostructure samples, the sample treated at lower temperature has the transition $^5D_0 \rightarrow {}^7F_2$ much more intense than the $^5D_0 \rightarrow {}^7F_1$, decreasing the intensity difference as the temperature grows. It is important to recall that the intensity of the magnetic dipole transition $^5D_0 \rightarrow {}^7F_1$ is not influenced by structural changes of the nearest neighborhood, typical of substitutional ions, while the transition $^5D_0 \rightarrow {}^7F_2$ is ruled by electric dipoles and is rather sensitive to the local crystalline field [19], the latter being easily identified when belonging to ions located at grain boundary layers, where the neighborhood changes from ion to ion. Then, the PL spectra of Fig. 5(a) allows interpreting that as the annealing temperature is increasing, the population of Eu^{3+} ions located at asymmetric sites (grain boundary sites) is decreasing, the Eu^{3+} ions becoming located preferentially at substitutional Sn sites for temperatures as high as 1000ºC. Fig. 5(b) is a very interesting result in this direction. The PL spectra for the heterostructure obtained with annealing at 200ºC is by far the most interesting, allowing identify several Eu^{3+} transitions, with the electric dipole ruled $^5D_0 \rightarrow {}^7F_2$ transition being the most intense. However, the other spectra bring some features that must be noticed. The heterostructure with top layer annealed at 300ºC by 1 hour (red line in Fig. 5(b)) still carries the $^5D_0 \rightarrow {}^7F_2$ transition and even traces of the $^5D_0 \rightarrow {}^7F_1$ magnetic dipole transition. As the temperature is increased to 400ºC (green line), the PL peaks decreases at little bit further, but still are clearly seen. For higher temperatures (annealing at 450 and 500ºC by 1 h), the peaks referring to the Eu^{3+} transitions, although still there, are seen only with some effort. The result in Fig. 5(b) corroborates with previous discussion in the sense that the $^5D_0 \rightarrow {}^7F_2$ transition has its intensity decreased as the temperatures increases, which means that more Eu^{3+} becomes preferentially located at symmetric substitutional sites.

Figure 5(c) shows the PL spectra for the GaAs/SnO_2:at.%Eu (0.05, 0.1) samples, annealed at 200°C by 1 hour, and GaAs/SnO_2:2%Eu annealed at 400°C by 20 min, with excitation by the 488 nm (2.53 eV) line from an Ar^+ laser, which has energy below the SnO_2 bandgap, assuring that no energy transfer from the matrix is responsible for the Eu^{3+} transitions. Four transitions were identified for these three samples: $^5D_0 \rightarrow {}^7F_0$, $^5D_0 \rightarrow {}^7F_1$, $^5D_0 \rightarrow {}^7F_2$ and $^5D_0 \rightarrow {}^7F_3$. Although $^5D_0 \rightarrow {}^7F_1$

and $^5D_0 \rightarrow {}^7F_2$ luminescent transitions are the most common, and are discussed in this paper, the other two have been reported [37-40]. In our data, some of these transitions were identified only by evaluating the first derivative as shown in the inset of Fig. 5(c), for Eu-doped heterostructures (0.05 and 0.1at.%Eu). The peak at 1.77 eV refers to the $^5D_0 \rightarrow {}^7F_4$ transition, being seen only in the GaAs/SnO_2:2%Eu heterostructure. This transition does not present pure magnetic dipole character or a pure electric dipole [39], even though it is predominantly electric dipole in character [41]. In the identification of Eu^{3+} bands in Ga_2O_3, the incident light has excitation energy of 2.54 eV, used for measurement done by Chen et al [37], also lower than the Ga_2O_3 matrix band gap (4.9 eV). Their hypothesis in this case is of electrons excitation from valence band to donor level (oxygen vacancy) by the light source. The related energy for the electron recombination in the defect state with the photogenerated holes can be transferred to the excited states of Eu ions, and the $^5D_0 \rightarrow {}^7F_4$ transition emission intensity of the Eu-doped films increases with the increase of Eu concentration. It is also important to mention that the broad band shown in Fig. 5(b) is not observed when the heterostructure samples are excited with below bandgap light, as the case of Fig. 5(c), which assures that the broad band and its temperature dependent features are a matrix related phenomenon. Figure 5(d) shows PL for SnO_2:2%Eu powder, with excitation by the 488 nm line from the Ar^+ laser. The inset shows PL for SnO_2:0.05%Eu powder. The emission related to Eu^{3+} transitions: $^5D_0 \rightarrow {}^7F_0$, $^5D_0 \rightarrow {}^7F_1$, $^5D_0 \rightarrow {}^7F_2$, $^5D_0 \rightarrow {}^7F_3$ and $^5D_0 \rightarrow {}^7F_4$ are all clearly identified, being more evident for the most doped sample. It is interesting to note that the broad band is not observed for powders as well, in agreement with the result observed previously for Kr^+-laser excitation [20].

Differences on Eu^{3+} PL spectra by exciting with light with energy above and below bandgap of the matrix have been reported by several relevant papers. Concerning Eu^{3+}-doped SnO_2 nanocrystals dispersed in SiO_2 matrix, Thanh et al. [42] inferred that excitation energy of 4.42 eV corresponds to the SnO_2 nanocrystal absorption band and the PL emissions can be assigned to the transfer of non-radiative energy between SnO_2 nanocrystals and Eu^{3+} ions, resulting in radiative $^5D_0 \rightarrow {}^7F_J$ transitions. The difference between the PL spectra is rather large when compared to excitation with 3.16 eV, mainly in the magnetic dipole $^5D_0 \rightarrow {}^7F_1$ radiative transition (2.10 eV). In indirect excitation (4.42 eV), PL spectra show well-resolved and intense emission band from

magnetic dipole $^5D_0 \rightarrow {}^7F_1$ transition. The emission band dominance from electric dipole $^5D_0 \rightarrow {}^7F_2$ transition can be seen only by direct excitation (3.16 eV). The authors assumed that a large number of optical active Eu^{3+} ions located in low-symmetry sites in SiO_2 matrix participate in direct excitation. The SnO_2 nanocrystals' number determines the PL intensity saturation levels from optically active Eu^{3+} ions by indirect excitation. A similar sort of excitation used in the present paper is used by Chen and coworkers [38] on Eu^{3+}-doped Ga_2O_3 films, deposited on sapphire substrates by pulsed laser deposition. The transitions from $^5D_0$ to $^7F_1$, $^7F_2$ and $^7F_3$, which are dominant for the emission of Eu, significantly decrease as the temperature increases by using 325 nm light (He-Cd laser), whereas excitation with 488 nm light (Ar^+ laser) leads to very week PL peaks, not detected from 77 to 200 K, becoming detectable above 200 K, thus increasing with temperature. The effect of the excitation wavelength upon the Eu^{3+} luminescence properties is also evaluated by Kolesnikov and coworkers [40], on Y_2O_3 nanoparticles matrix. The effect of 4 excitation energies on the PL spectra is investigated. Intense emission of nanoparticles was attributed to Eu^{3+} transitions occurring between the $^5D_0$ excited state and ^7F_J ground states and the most efficient emission was activated by transfer of energy between Eu^{3+} and O^{2-} and subsequent energy transfer to the doping ions.

As already mentioned, either the main as the secondary features in the XANES show that there are differences in the Eu site neighborhood for the SnO_2:Eu thin films and heterostructures, and they may affect the luminescence, since it can be directly affected by the electron-phonon coupling. The local crystalline structure leads to the change in the intensity of this coupling, which varies from site to site, so the difference in structure affects the luminescence spectra [43]. The geometry and the organization of local environmentof the analyzed ion influence the electron-phonon interaction. The combination of SnO_2:Eu with GaAs allows the presence of smaller crystallites than for the SnO_2:Eu samples for similar annealing temperatures. Besides, the higher the thermal annealing temperature, the larger the crystallite size in these samples [20]. Then, the influence of annealing temperature on the main Eu^{3+} emission lines, as already discussed, may be associated with the crystallite size. For smaller crystallites the ion is located mainly at grain boundary, with the dominant transition $^5D_0 \rightarrow {}^7F_2$ (about 2.0 eV), as the grain grows Eu^{3+} ions

become preferentially located inside the crystallite substitutional to Sn^{4+}, with the dominant transition $^5D_0 \rightarrow {}^7F_1$ (about 2.1 eV). Eu^{3+} emission peaks were observed only for samples deposited on GaAs, these heterostructures in addition to being more rigid are more organized when compared to the SnO_2:Eu films. Then, they have a better environment for luminescence.

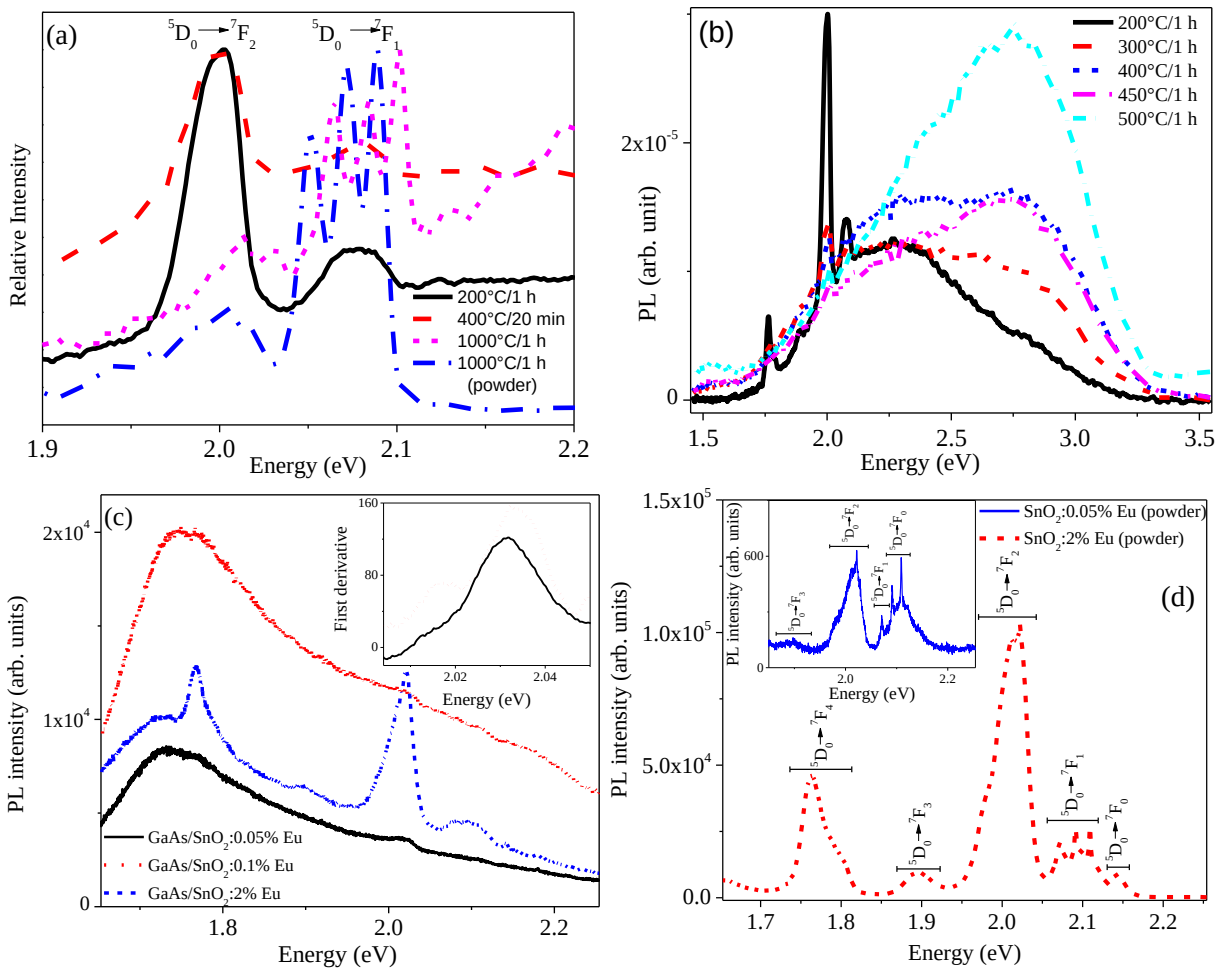

Fig.5. (a) PL relative intensity with magnification of $^5D_0 \rightarrow {}^7F_1$ and $^5D_0 \rightarrow {}^7F_2$ emission peaks of GaAs/SnO_2:2%Eu heterostructure thermally annealed at 200°C and at 400°C and SnO_2:2%Eu film and powder with thermal annealing of 1000°C.**(b)** PL of heterostructure with distinct thermal annealing: 200, 300, 400, 450 and 500°C by 1 h .**(c)** PL for GaAs/SnO_2:0.05%Eu and GaAs/SnO_2:0.1%Eu annealed at 200°C and GaAs/SnO_2:2%Eu annealed at 400°C by 20 min. **Inset:** First derivative curves of GaAs/SnO_2:0.05%Eu and GaAs/SnO_2:0.1%Eu. **(d)** PL for SnO_2:2%Eu powder. **Inset:** PL for SnO_2:0.05%Eu powder. Excitation: **(a)** and **(b)**: line 350 nm of the Kr^+ laser, (c) and (d): line 488 nm of the Ar^+ laser.

Fig. 6 (a) shows Raman spectra of SnO_2:0.05%Eu and SnO_2:2%Eu powders, and the inset is the Raman spectra of the heterostructures GaAs/SnO_2:0.05%Eu, GaAs/SnO_2:0.1%Eu and GaAs/SnO_2:2%Eu. SnO_2 has a tetragonal crystalline system and a rutile type structure. The unit cell has six atoms, two tin and four oxygen, yielding 18 branches for the vibrational modes in the first Brillouin zone [44]: four are Raman active (three non-degenerate modes A_{1g}, B_{1g}, B_{2g}, and the double degenerate E_g), two are silent (A_{2g} and B_{1u}) and two are activated in infrared (A_{2u} and triple degenerate E_u). One A_{2u} and two E_u are acoustic modes [44]. Oxygen atoms vibrate while tin atoms are at rest in the Raman active modes. The non-degenerate modes A_{1g}, B_{1g} and B_{2g} vibrate in the *c*-axis perpendicular plane, and the double degenerate E_g mode vibrates in the *c*-axis direction [44]. Analyzing Fig. 6(a), which refers to Raman spectra for powders, six vibration modes of SnO_2 were identified: B_{1g} (115-123 cm^{-1} [45]), E_g (475-478 cm^{-1} [45,46]), A_{1g} (632-635 cm^{-1} [45,46]), (A_{2u}) $\nu_{3(LO)}$ (687-693 cm^{-1} [44]) and B_{2g} (773-777 cm^{-1} [43,44]), which confirms the tetragonal rutile structure of SnO_2 [45], besides the peak located at about 304 cm^{-1}, which can be associated with the surface modes of SnO_2 nanostructures [47]. E_g is related to the vibration of oxygen in this plane, while A_{1g} and B_{2g} are related to the vibrational modes' expansion and contraction in Sn–O bonds. In B_{2g} mode, the six Sn–O bonds contract coordinately at the same time, leading to a higher repulsive force of the O–O bonds, and in A_{1g} mode, two bonds contract and four bonds expand or contract in opposite directions [45]. Fig. 6(b) shows the Raman spectra of the 0.05, 0.1 and 2at.%Eu-doped heterostructures. The GaAs/SnO_2:0.05%Eu heterostructure have two SnO_2 vibration modes, A_{2g} (390 cm^{-1} [46]) and (A_{2u}) $\nu_{(TO)}$ (497-512 cm^{-1} [46]), and one Eu_2O_3 vibration mode at about 285 cm^{-1} due to stretching vibration modes of Eu–O bonds [48]. The GaAs/SnO_2:0.1%Eu heterostructure have one SnO_2 vibration mode, (A_{2u})$\nu_{(TO)}$ (497-512 cm^{-1} [46]), and three Eu_2O_3 vibration modes at about 109 cm^{-1} [49], about 140 cm^{-1} [49] and about 285 cm^{-1} [48]. The GaAs/SnO_2:2%Eu have two SnO_2 vibration modes, B_{1g} (115-123 cm^{-1} [49]) and (A_{2u}) $\nu_{(TO)}$ (497-512 cm^{-1} [46]), and two Eu_2O_3 vibration mode at about 140 cm^{-1} [49] and 285 cm^{-1} [48]. Below 300 cm^{-1} there are two evident experimental peaks at 265 cm^{-1} and 285cm^{-1}. Abrashev et al [50] found a peak at 289 cm^{-1} related to

$E_g + F_g$ vibration of Eu_2O_3 whereas Irshad et. al [51] found and asymmetric Eu_2O_3 band at 285 cm^{-1}. On the other hand, GaAs bands are also located in this spectral range, and peaks are located about 265 cm^{-1} and 290 cm^{-1}, and refers to the active TO and LO Raman modes of the GaAs layer [52-54]. As discussed in this paper and in previous publication [20], the GaAs bottom layer favor the showing up of Eu agglomerates, which would justify the Eu_2O_3 modes. Concerning the GaAs modes, they are in good agreement with the X-ray results (Fig. 4) which present more intense GaAs peaks, even though the GaAs is the bottom layer, and some SEM features (Fig 1(f)), which show regions where the GaAs surface clearly appears.

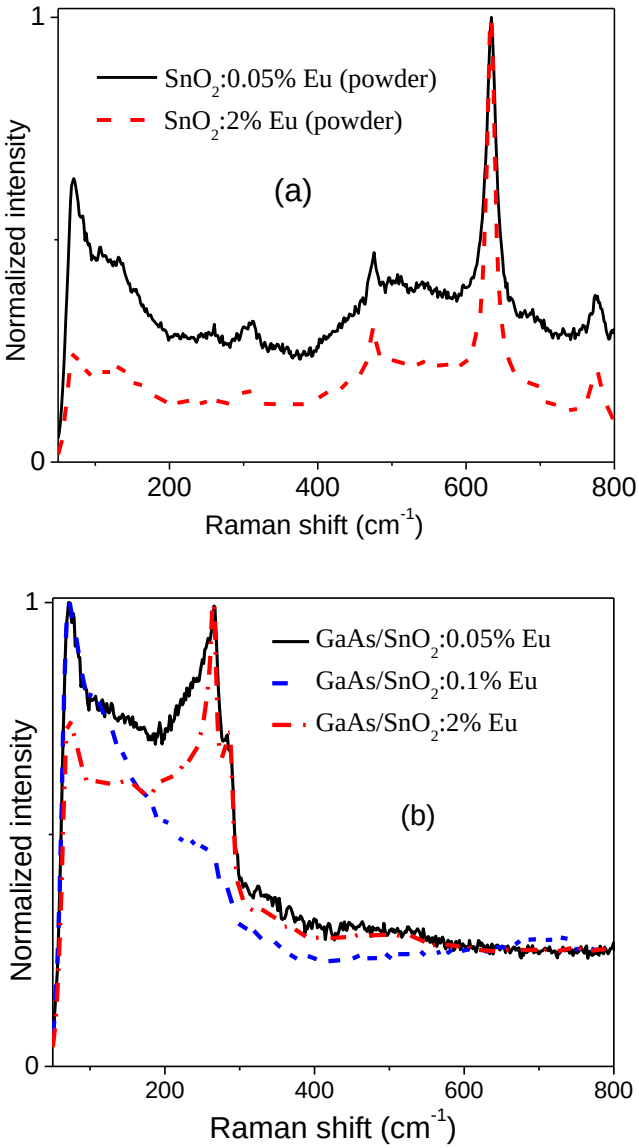

Fig. 6. **(a)** Raman spectra of SnO_2:0.05%Eu and SnO_2:2%Eu powders. **(b)** Raman spectra of GaAs/SnO_2:0.05%Eu, GaAs/SnO_2:0.1%Eu and GaAs/SnO_2:2%Eu heterostructures.

3.3 Some electrical characteristics

It is well known that photoconductivity may be largely increased in a semiconductor by irradiating with appropriated wavelength light. The GaAs/SnO_2 heterostructure has been excited with below SnO_2 bandgap light from an InGaN LED (450 nm) and with a He-Cd laser (325 nm), which is just above the SnO_2 band gap energy (SnO_2 is the top layer, which is illuminated by the light incidence). These excitations followed by the respective current decay have been explored for investigating the carrier trapping by defects, giving birth to a recent paper on a modeling where the heterostructure interface trapping as well as the Eu^{3+} agglomerates play fundamental roles [25]. The decay of persistent photoconductivity in semiconductors and heterostructures have been reviewed recently [26], and are successfully applied for defects subject to some local lattice relaxation [55-57]. The relevance of its application is to electrically characterize these heterostructure samples in order to understand the electro-optical phenomena in this sort of semiconductor assembly and then, contribute for optoelectronic devices operation. However, the scope here is not to apply this experiment again to this heterostructure but to show some facets not reported before.

The observed photo-induced current decay for the heterostructure GaAs/SnO_2:2%Eu, with the described excitations, leads to temperature dependent magnitude, and is slower as the temperature is increased [25], which although similar to Sb-doped SnO_2 films [58], is a surprising result, because the trapping by defects is a thermally activated process, and for higher temperature the decay should be faster as observed for Er and Eu-doped SnO_2 [57,59], besides the shape of the decay curve shows dependence with light source, mainly at lower temperature [25,26].

Fig. 7(a) is a diagram of the heterostructure sample structure along with the electric polarization scheme during the photo-induced conductivity decay measurement. It is used here to measure the dark current, just before photoexcitation and to measure again after the transient current decay has finished. Black balls represent electrons which are under movement in the SnO_2 top layer due to bias, or are trapped at GaAs/SnO_2 interface.

Fig. 7(b) represents the variation on sample resistivity for measurements before excitation (in the dark) and after the complete decay, which is obtained when the current becomes stationary

again. It is obtained from current-voltage measurements as seen in the Figs. 7(c) and 7(d). Fig. 7(c) is the current-voltage behavior before excitation with the InGaN LED, and after current decay at 200 K. Fig 7(d) is the current-voltage curve before excitation with the same source and after decay at 50 K. In this last case only the positive part is plotted since the behavior is ohmic for the whole temperature range, similar to what is seen in the Fig. 7(c). As can be seen, there is a permanent variation on resistivity for lower temperature, which is an indication of persistent photoconductivity (PPC) portion, even though the decay is rather faster for lower temperature. At 200 K, the variation in resistivity is negligible, mainly for illumination with the InGaN LED (blue balls) indicating that the PPC is no longer a fact. Another interesting feature seen in Fig. 7(b) is that the InGaN LED leads to a more permanent portion on the resistivity variation (blue symbols) as the temperature decreases (1/T increases), whereas the He-Cd laser leads to a practically constant value as the temperature decreases (red symbols). This is a good indication that the intrabandgap states, predominantly excited by the LED, have a thermally activated cross section, typical of large lattice relaxation defects [55,56], meaning that as the temperature increases the thermal trapping becomes considerable, and the PPC is destroyed.

The energy of the used laser is above the SnO_2 bandgap energy, then more excited carriers are expected, including electron-hole pair generation. Electrons may be excited to overcome the potential barrier at the heterostructure interface, becoming located at the GaAs side, which may return very slowly to the equilibrium state [25, 26]. Then, at low temperature, the PPC is less evidenced for the excitation with the laser, since a significant part of the excited electrons does not take part in the conduction process, because they are trapped at the GaAs/SnO_2 interface. On the other hand, as the temperature increases the PPC is much more evident for excitation with the laser. Trapping at the interface leads to a slower retrapping back compared to SnO_2 intrabandgap excitation with the LED. In the case of InGaN LED excitation, the continuously decreasing permanent portion of conductivity means that only the intrabandgap defects are excited and the electrons are raised to a lower energy state, remaining in the heterostructure SnO_2 side. These electrons do not have enough thermal energy to overcome the interface potential barrier [25,26]. LED excitation (energy of 2.76 eV) is in good agreement with the PL data which show a broad

band originated from a transition between Eu^{3+} acceptors and oxygen vacancy donors [20]. It explains why the LED energy does not excite electrons to overcome the interface potential barrier, because the Eu^{3+} acceptors are located deeper in the bandgap, closer to the valence band.

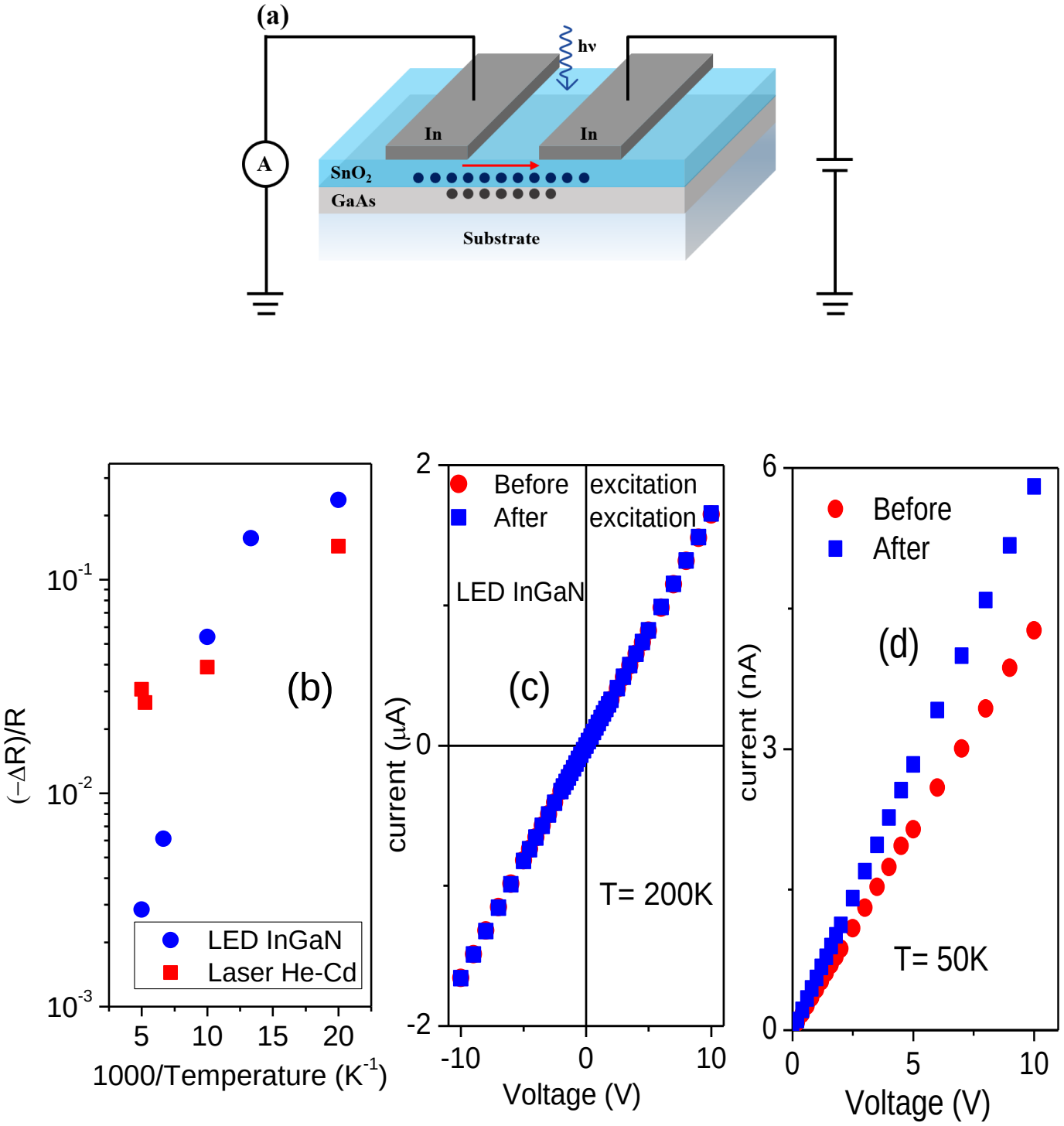

Fig. 7. (a) Diagram of the heterostructure sample structure and polarization procedure during electrical characterization. (b) Variation on sample resistivity for measurements before excitation (in the dark) and after the complete decay (600 s) for heterostructure GaAs/SnO_2:2%Eu treated at 200°C/1 h.**(c)** Current-

voltage curve before excitation with the InGaN LED and after current decay, at 200 K. **(d)** Current-voltage curve before excitation with the InGaN LED and after decay, at 50 K.

4. Conclusions

The differences between the XANES data for GaAs/SnO_2 heterostructure samples and for Eu-doped SnO_2 thin films, deposited on glass substrate, are interpreted as responsible for the differences in the PL spectra concerning the Eu^{3+} emission, since films deposited on glass substrate does not present Eu^{3+} PL transitions until the annealing temperature is rather high.

The relative intensity of the Eu^{3+} transitions $^5D_0 \rightarrow {}^7F_1$ (substitutional to Sn^{4+} sites) and $^5D_0 \rightarrow {}^7F_2$ (grain boundary located) changes as the annealing temperature increases. For the heterostructure samples where the SnO_2 layer is treated up to 400ºC, the transition $^5D_0 \rightarrow {}^7F_2$ is the most intense, whereas for the samples treated at 1000ºC the $^5D_0 \rightarrow {}^7F_1$ is clearly the most intense. This can be associated with increase on the concentration of symmetric sites with temperature, which also affects the crystallite growth.

Besides the Eu^{3+} emission, the PL spectra of heterostructures also display a broad band, which is only present for excitation with above bandgap light (350 nm from a Kr^+ laser), and it is blue-shifted as the annealing temperature increases. This broad band is associated with electron transition between oxygen vacancy donors and Eu^{3+} acceptors. This broad band is not observed for excitation with the 488 nm line of an Ar^+ laser, which has below band gap energy. The main and secondary features in the XANES data show that there are differences in the average local Eu environment for the SnO_2:Eu thin films and heterostructures: a more ordered average site for Eu in the heterostructures.

Sample resistivity measured in the dark and just after a photo-induced current decay has finished evidences that photo-ionized intrabandgap states, mainly acceptor levels, are responsible for the persistent photoconductivity in the heterostructures.

Results reported here are contributions to the understanding of the optical and optically excited electrical properties of the heterostructure GaAs/SnO_2 in the form of thin films. This format for the samples makes possible the integration of this assembly in optoelectronic systems.

Acknowledgements

The authors thank Brazilian financial sources: CNPq, CAPES (Process: 88881.131882/2016-01 and 88887.375016/2019-00 - CAPES-PRINT). Besides, they thank Prof. Maximo S. Li for the help with some of the Kr^+ excited PL data, Antonio R. Zanatta for the PL measurements with the Ar^+ laser and Prof. Dayse I. Santos for X-ray diffraction experiments at Multiuser equipment lab.

Additional Information

Conflict of Interests: The authors declare no conflict of interests.

References

[1] Franco Jr A, Pessoni HVS, Ribeiro PRT, Machado FLA (2017) Magnetic properties of Co-doped ZnO nanoparticles. J Magn Magn Mater 426**:**347-350. https://doi.org/10.1016/j.jmmm.2016.10.159

[2] Zhang L, Yu W, Han C, Guo J, Zhang Q, Xie H, Shao Q, Sun Z, Guo Z (2017) Large scaled synthesis of heterostructured electro spun TiO_2/SnO_2 nanofibers with an enhanced photocatalytic activity. J Electrochem Soc 164:H651-H656. https://doi.org/10.1149/2.1531709jes

[3] Yang Y, Li S, Liu F, Zhang N, Liu K, Wang S, Fang G (2017) Bidirectional electroluminescence from p-SnO_2/i-MgZnO/n-ZnO heterojunction light-emitting diodes. J Lumin186:223-228. https://doi.org/10.1016/j.jlumin.2017.02.043

[4] Bouras K, Schmerber G, Rinnert H, Aureau D, Park H, Ferblantier G, Colis S, Fix T, Park C, Kim WK, Dinia A, Slaoui A (2016) Structural, optical and electrical properties of Nd-doped

SnO_2 thin films fabricated by reactive magnetron sputtering for solar cell devices. Sol Energy Mater Sol Cells145:134-141.https://doi.org/10.1016/j.solmat.2015.07.038

[5] Ammari A, Trari M, Zebbar N (2019) Materials science in semiconductor processing transport properties in Sb-doped SnO_2 thin films: Effect of UV illumination and temperature dependence. Mat Sci Semicon Proc 89:97-104.https://doi.org/10.1016/j.mssp.2018.09.003

[6] Martinez-Gazoni RF, Allen MW, Reeves RJ (2018) Conductivity and transparency limits of Sb-doped SnO_2 grown by molecular beam epitaxy. Phys Rev B 98:155308(10). https://doi.org/10.1103/PhysRevB.98.155308

[7] Park M, Kim J-Y, Son HJ, Lee C-H, Jang SS, Ko MJ (2016) Low-temperature solution-processed Li-doped SnO_2 as an effective electron transporting layer for high-performance flexible and wearable perovskite solar cells. Nano Energy 26:208-215. https://doi.org/10.1016/j.nanoen.2016.04.060

[8] Wang Y, Chen T (2009) Nonaqueous and template-free synthesis of Sb doped SnO_2 microspheres and their application to lithium-ion battery anode. Electrochim Acta 54:3510-3515. https://doi.org/10.1016/j.electacta.2008.11.039

[9] Ghaitaoui T, Benatiallah A,Sahli Y,Khachab H (2018) Realization and characterization of p-typed polythiophene based organic photovoltaic cells. J Nano- Electron Phys 10:01008(5). https://doi.org/10.21272/jnep.10(1).01008

[10] Eliseeva SV, Büznli J-CG (2010) Lanthanide luminescence for functional materials and bio-sciences. Chem Soc Rev 39:189-227. https://doi.org/10.1039/B905604C

[11] Mrázek J, Surýnek M, Bakardjieva S, Buršík J, Kašík I (2014) Synthesis and crystallization mechanism of europium-titanate $Eu_2Ti_2O_7$. J Cryst Growth 391:25-32. https://doi.org/10.1016/j.jcrysgro.2013.12.045

[12] Gurman SJ (2001) Amorphous materials: X-ray absorption spectroscopy. In: Buschow KHJ, Cahn RW, Flemings MC, Ilschner B, Kramer EJ, Mahajan S, Veyssière P (ed) Encyclopedia of materials: Science and technology, 1st edn. Elsevier Science & Technology, London, pp 256-259

[13] Amidani L, Korthout K, Joos JJ, van der Linden M, Sijbom HF, Meijerink A, Poelman D, Smet PF, Glatzel P (2017) Oxidation and luminescence quenching of europium in $BaMgAl_{10}O_{17}$ blue phosphors. Chem Mater 29:10122-10129. https://doi.org/10.1021/acs.chemmater.7b03918

[14] Farias AM, Sandrini M, Viana JRM, Baesso ML, Bento AC, Rohling JH, Guyot Y, Ligny D, Nunes LAO, Gandra FG, Sampaio JA, Lima SM, Andrade LHC, Medina AN (2015) Emission tunability and local environment in europium-doped OH^--free calcium alumino silicate glasses for artificial lighting applications. Mater Chem Phys 156:214-219. https://doi.org/10.1016/j.matchemphys.2015.03.002

[15] Grzeta B, Lützenkirchen-Hecht D, Vrankic M, Bosnar S, Saric A, Takahashi M, Petrov D, Biscan M (2018) Environment of the Eu^{3+} ion within nanocrystalline Eu-doped $BaAl_2O_4$: Correlation of X-ray diffraction, Mössbauer spectroscopy, X-ray absorption spectroscopy, and photoluminescence investigations. Inorg Chem 57:1744-1756. https://doi.org/10.1021/acs.inorgchem.7b02322

[16] Layek A, Yildirim B, Ghodsi V, Hutfluss LN, Hegde M, Wang T, Radovanovic PV (2015) Dual europium luminescence centers in colloidal Ga_2O_3 nanocrystals: Controlled *in situ* reduction of Eu(III) and stabilization of Eu(II). Chem Mater 27:6030 6037. https://doi.org/10.1021/acs.chemmater.5b02383

[17] Menushenkov AP, Yaroslavtsev AA, Geondzhian AY, Chernikov RV, Nataf L, Tan X, Shatruk M (2017) Driving the europium valence state in $EuCo_2As_2$ by external and internal impact. J Supercond Nov Magn 30:75-78. https://doi.org/10.1007/s10948-016-3771-0

[18] Ishii M, Komuro S, Morikawa T (2003) Study on atomic coordination around Er doped into anatase- and rutile- TiO_2:Er−O clustering dependent on the host crystal phase. J Appl Phys 94:3823-3827.https://doi.org/10.1063/1.1602567

[19] Morais EA, Scalvi LVA, Tabata A, Oliveira JBB, Ribeiro SJL (2008) Photoluminescence of Eu^{3+} ion in SnO_2 obtained by sol-gel. J Mater Sci 43:345-349. https://doi.org/10.1007/s10853-007-1610-1

[20] Bueno CF, Scalvi LVA, Li MS, Saeki MJ (2015) Luminescence of Eu^{3+} in the thin film heterojunction GaAs/SnO_2.Opt Mater Express 5:59-72. https://doi.org/10.1364/OME.5.000059

[21] Pineiz TF, Scalvi LVA, Saeki MJ, Morais EA (2010) Interface formation and electrical transport in SnO_2:Eu^{3+}/GaAs heterojunction deposited by sol-gel dip-coating and resistive evaporation. J Electron Mater 39:1170-1176. https://doi.org/10.1007/s11664-010-1161-0

[22] Pineiz TF, Morais EA, Scalvi LVA, Bueno CF (2013) Interface formation of nanostructured heterojunction SnO_2:Eu/GaAs and electronic transport properties. Appl Surf Sci 267:200-205. https://doi.org/10.1016/j.apsusc.2012.10.097

[23] Bueno CF, Scalvi LVA (2016) On the electrical properties of distinct Eu^{3+} emission centers in the heterojunction GaAs/SnO_2. Thin Solid Films 612:303-309. https://doi.org/10.1016/j.tsf.2016.06.008

[24] Machado DHO, Scalvi LVA, Tabata A, Silva JHD (2017) Interface conduction and photo-induced electrical transport in the heterojunction formed by GaAs and Ce^{3+}-doped SnO_2.J Mater Sci: Mater Electron 28:5415-5424. https://doi.org/10.1007/s10854-016-6202-x

[25] Bueno CF, Scalvi LVA (2018) Electron trapping in the photo-induced conductivity decay in GaAs/SnO_2 heterostructure. Appl Phys A 124:457(12). https://doi.org/10.1007/s00339-018-1874-0

[26] Scalvi LVA, Bueno CF (2020) Transient decay of photoinduced current in semiconductors and heterostructures. J Phys D: Appl Phys 53:033001(23). https://doi.org/10.1088/1361-6463/ab495a

[27] Wang Y, Ma J, Si F, Yu X, Ma H (2005) Structural and photoluminescence characters of SnO_2:Sb films deposited by RF magnetron sputtering. J Lumin114:71-76. https://doi.org/10.1016/j.jlumin.2004.12.003

[28] Geraldo V, Briois V, Scalvi LVA, Santilli CV (2010) Structural characterization of nanocrystalline Sb-doped SnO_2xerogels by multiedge X-ray absorption spectroscopy. J Phys Chem C114:19206-19213. https://doi.org/10.1021/jp106001x

[29] Proux O, Lahera E, Del Net W, Kieffer I, Rovezzi M, Testemale D, Irar M, Thomas S, Aguilar-Tapia A, Bazarkina EF, Prat A, Tella M, Auffan M, Rose J, Hazemann J-L (2017) High-Energy Resolution Fluorescence Detected X-Ray Absorption Spectroscopy: A powerful new structural tool in environmental biogeochemistry sciences. J Environ Qual Abstract - Special Section: Synchrotron Radiation-Based Methods For Environmental Biogeochemistry 46:1146-1157. https://doi.org/10.2134/jeq2017.01.0023

[30] Figueroa SJA, Maurício JC, Murari J, Beniz DB, Piton JR, Slepicka HH, Sousa MF, Espíndola AM, Levinsky APS (2016) Upgrades to the XAFS2 beamline control system and to the endstation at the LNLS. J Phys Conf Ser 712:012022(4). https://doi.org/10.1088/1742-6596/712/1/012022

[31] Ravel B, Newville M (2005) ATHENA, ARTEMIS, HEPHAESTHUS: Data analysis for X-ray absorption spectroscopic using IFEFFIT. J Synchrotron Radiat 12:537-541. https://doi.org/10.1107/S0909049505012719

[32] Gaillard C, Billard I, Chaumont A, Mekki S, Ouadi A, Denecke MA, Moutiers G, Wipff G (2005) Europium(III) and its halides in anhydrous room-temperature imidazolium-based ionic liquids: A combined TRES, EXAFS, and molecular dynamics study. Inorg Chem 44:8355-8367. https://doi.org/10.1021/ic051055a

[33] Korthout K, Parmentier AB, Smet PF, Poelman D (2013) A XAS study of the luminescent Eu centers in thiosilicate phosphors. Phys Chem Chem Phys15:8678-8683. https://doi.org/10.1039/C3CP44334E

[34] Ray SC, Karanjai MK, Dasgupta D (1998) Tin dioxide based transparent semiconducting films deposited by the dip-coating technique. Surf Coat Tech 102:73-80. https://doi.org/10.1016/S0257-8972(97)00561-6

[35] JCPDS - Joint Committee on Powder Diffraction Standards/ International Center for Diffraction Data – ICDD, Powder Diffraction File, Pennsylvania: JCPDS/ICDD, 2003. https://www.icdd.com/pdfsearch/

[36] Marotti RE, Giorgi P, Machado G, Dalchiele EA (2006) Crystallite size dependence of band gap energy for electrodeposited ZnO grown at different temperatures. Sol Energy Mater Sol Cells 90:2356-2361. https://doi.org/10.1016/j.solmat.2006.03.008

[37] Chen Z, Saito K, Tanaka T, Nishio M, Arita M, Guo Q (2015) Low temperature growth of europium doped Ga_2O_3 luminescent films. J Cryst Growth 430:28-33. https://doi.org/10.1016/j.jcrysgro.2015.08.020

[38] Chen Z, Wang X, Zhang F,Noda S, Saito K, Tanaka T, Nishio M, Guo Q (2016) Temperature dependence of luminescence spectra in europium doped $6a_2O_3$ film. J Lumin 177:48-53. https://doi.org/10.1016/j.jlumin.2016.04.013

[39] Gupta SK, Reghukumar C, Kadam RM (2016) Eu^{3+} local site analysis and emission characteristics of novel $Nd_2Zr_2O_7$:Eu phosphor: insight into the effect of europium concentration on its photoluminescence properties. RSC Adv 6:53614-53624. https://doi.org/10.1039/C6RA11698A

[40] Kolesnikov IE, Povolotskiy AV, Mamonova DV, Lähderanta E, Manshina AA, Mikhailov MD (2016) Photoluminescence properties of Eu^{3+} ions in yttrium oxide nanoparticles: defect vs. normal sites. RSC Adv 6:76533-76541. https://doi.org/10.1039/C6RA16814K

[41] Richardson FS (1982) Terbium(III) and europium(III) ions as luminescent probes and stains for biomolecular systems. Chem Rev 82:541-552. https://doi.org/10.1021/cr00051a004

[42] Thanh BQ, Ha NN, Khiem TN, Chien ND (2015) Correlation between SnO_2 nanocrystals optical properties of Eu^{3+} ions in SiO_2 matrix: Relation of crystallinity, composition, and photoluminescence. J Lumin 163:28-31. https://doi.org/10.1016/j.jlumin.2015.03.002

[43] Luo Z, Huang Y, Chen X (2007) Spectroscopy of solid-state laser and luminescent materials. Nova Science Publisher Inc., New York

[44] Diéguez A, Romano-Rodríguez A, Vilà A, Morante JR (2001) The complete Raman spectrum of nanometric SnO_2 particles. J Appl Phys 90:1550-1557. https://doi.org/10.1063/1.1385573

[45] Sangeetha P, Sasirekha V, Ramakrishnan V (2011) Micro-Raman investigation of tin dioxide nanostructured material based on annealing effect. J Raman Spectrosc 42:1634-1639. https://doi.org/10.1002/jrs.2919

[46] Lupan O, Chow L, Chai G, Schulte A, Park S, Heinrich H (2009)A rapid hydrothermal synthesis of rutile SnO_2 nanowires. Mater Sci Eng B157:101-104. https://doi.org/10.1016/j.mseb.2008.12.035

[47] Zuo J, Xu C, Liu X, Wang C, Hu Y, Qian Y (1994) Study of the Raman spectrum of nanometer SnO_2. J Appl Phys 75:1835-1836. https://doi.org/10.1063/1.356348

[48] Diallo A, Mothudi BK, Manikandan E, Maaza M (2016) Luminescent Eu_2O_3 nanocrystals by Aspalathus linearis' extract: structural and optical properties. J Nanophotonics 10:026010(12). https://doi.org/10.1117/1.JNP.10.026010

[49] Kumar S, Prakash R, Choudhary RJ, Phase DM (2015) Structural, XPS and magnetic studies of pulsed laser deposited Fe doped Eu_2O_3 thin film. Mater Res Bull 70:392-396. https://doi.org/10.1016/j.materresbull.2015.05.007

[50] Abrashev MV, Todorov ND, Geshev J (2014) Raman spectra of R_2O_3 (R-rare earth) sesquioxides with C-type bixbyite crystal structure: A comparative study. J Appl Phys 116:103508(7).https://doi.org/10.1063/1.4894775

[51] Irshad KA, Chandra Shekar NV, Ravindran TR, Srihari V, Pandey KK (2017) X-ray diffraction and Raman studies on Ho: Eu_2O_3. J Mol Struct 1128:325-329. https://doi.org/10.1016/j.molstruc.2016.08.077

[52] Dushaq G, Nayfeh A, Rasras M (2019) Complementary metal oxide semiconductor (CMOS) compatible gallium arsenide metal-semiconductor-metal photodetectors (GaAs MSMPDs) on silicon using ultra-thin germanium buffer layer for visible photonic applications. J Appl Phys 126:193106(10).https://doi.org/10.1063/1.5120705

[53] Evans DJ, Ushioda S, McMullen JD (1973) Raman Scattering from Surface Polaritons in a GaAs Film. Phys Rev Lett 31:369-372. https://doi.org/10.1103/PhysRevLett.31.369

[54] Sathasivam S, Arnepalli RR, Bhachu DS, Lu Y, Buckeridge J, Scanlon DO, Kumar B, Singh KK, Visser RJ, Blackman CS, Carmalt CJ (2016) Single step solution processed GaAs thin films from $GaMe_3$ and $^tBuAsH_2$ under ambient pressure. J Phys Chem C 120:7013-7019. https://doi.org/10.1021/acs.jpcc.6b00850

[55] Lang DV, Logan RA (1977) Large-lattice-relaxation model for persistent photoconductivity in compound semiconductors. Phys Rev Lett 39:635 639. https://doi.org/10.1103/PhysRevLett.39.635

[56] Dobson TW, Scalvi LVA, Wager JF (1990) Transient decay of persistent photoconductivity in $Al_{0.3}Ga_{O.7}As$. J Appl Phys 68:601-605. https://doi.org/10.1063/1.346785

[57] Morais EA, Scalvi LVA (2007) Electron trapping of laser-induced carriers in Er-doped SnO_2 thin films. J Eur Ceram Soc 27:3803-3806. https://doi.org/10.1016/j.jeurceramsoc.2007.02.037

[58] Floriano EA, Scalvi LVA , Sambrano JR, Andrade A (2013) Decay of photo-induced conductivity in Sb-doped SnO2 thin films, using monochromatic light of about bandgap energy. Appl. Surf. Sci. 267:164-168. https://doi.org/10.1016/j.apsusc.2012.09.003

[59] Morais EA, Scalvi LVA, Cavalheiro AA, Tabata A, Oliveira JBB (2008) Rare earth centers properties and electron trapping in SnO_2 thin films produced by sol-gel route. J Non-Cryst Solids 354:4840-4845. https://doi.org/10.1016/j.jnoncrysol.2008.04.029